nature communications

Article

https://doi.org/10.1038/s41467-024-54844-4

Diffusion limited synthesis of wafer-scale covalent organic framework films for adaptative visual device

Received: 1 March 2024

Accepted: 21 November 2024

Published online: 02 December 2024

Check for updates

Minghui Liu[1,2,6], Junhua Kuang[1,2,6], Xiaocang Han[3], Youxing Liu[1,2], Wenqiang Gao[1,2], Shengcong Shang[1,2], Xinyu Wang[1,2], Jiaxin Hong[1,2], Bo Guan[1], Xiaoxu Zhao[3] ✉, Yunlong Guo[1,2] ✉, Jichen Dong[1,2] ✉, Zhiyuan Zhao[1], Yan Zhao[4], Chuan Liu[5], Yunqi Liu[1,2] & Jianyi Chen[1,2] ✉

Synthesizing high-crystalline covalent organic framework films is highly desired to advance their applications in two-dimensional optoelectronics, but it remains a great challenge. Here, we report a diffusion-limited synthesis strategy for wafer-scale uniform covalent organic framework films, in which pre-deposited 4,4′,4″,4‴-(1,3,6,8-Tetrakis(4-aminophenyl) pyrene is encapsulated on substrate surface with a layer of covalent organic framework pre-polymer. The polymer not only prevents the dissolution of precursor, but limits the reaction with terephthalaldehyde dissolved in solution, thereby regulating the polymerization process. The size depends on growth substrates, and 4-inch films have been synthesized on silicon chips. Their structure, thickness, patterning and crystallization degree can be controlled by adjusting building blocks and polymerization chemistries, and molybdenum disulfide have been used as substrates to construct vertical heterostructure. The measurements reveal that using covalent organic framework as a photosensitive layer, the heterojunction displays enhanced photoelectric performance, which can be used to simulate the adaptative function of visual system.

With the continuous development of technology, it has become a consensus to develop novel biomimetic devices for simulating the physiological functions of organisms[1–4]. Among them, the development of bionic artificial visual perception devices is necessary for future autonomous driving as well as for applications in a wide range of lighting scenarios[5–7]. Inorganic PbS quantum dots and graphene have been used to construct light intensity-adaptive photodetector to achieve tunable adaptation accuracy and controllable adaptation sensitivity[6]. However, stability and biocompatibility issues based on quantum dots are an unavoidable problem. It has become an important issue to develop new materials that are both acid and alkali-resistant and biocompatible. Covalent organic frameworks (COFs) constructed via strong covalent bonds are an emerging class of advanced porous polymers[8–11]. The materials have superior potential in gas sensors[12], drug delivery[13,14] and catalysis applications due to their excellent chemical stability, well-defined skeletons, large specific surface area and tailored functionalities[15–18]. In particular, two-dimensional (2D) COFs with stacking layers allow charge carrier transport along an extended π-conjugation plane or through space-aligned molecular columns[19–26]. When graphene and transition metal

[1]Beijing National Laboratory for Molecular Sciences, Key Laboratory of Organic Solids, Institute of Chemistry, Chinese Academy of Sciences, Beijing 100190, P. R. China. [2]University of Chinese Academy of Sciences, Beijing 100049, P. R. China. [3]School of Materials Science and Engineering, Peking University, Beijing 100871, P. R. China. [4]Department of Materials Science, Fudan University, Shanghai 200433, P. R. China. [5]State Key Laboratory of Optoelectronic Materials and Technologies, Guangdong Province Key Laboratory of Display Material and Technology, School of Electronics and Information Technology, Sun Yat-sen University, Guangzhou 510275, P. R. China. [6]These authors contributed equally: Minghui Liu, Junhua Kuang. ✉e-mail: xiaoxuzhao@pku.edu.cn; guoyunlong@iccas.ac.cn; dongjichen@iccas.ac.cn; chenjy@iccas.ac.cn

dichalcogenides (TMDs) were assembled into heterostructure with 2D COFs through van der Waals (vdW) interactions[27–31], in addition to finding applications in flexible optoelectronic devices, emergent phenomena were produced which were not observed in individual building blocks due to quantum confinement effect. However, the performance of COF films in optoelectronic applications is compromised due to charge build-up, phonon scattering and signal propagation delay as a consequence of the level of crystallinity and surface defects such as cracks, bulges, and crumbling in COF films[32–34]. Therefore, constructing 2D crystalline COF films for optoelectronic devices is highly desired, and has been a long-sought aim of chemists.

A typical synthesis of COF typically consists of vacuum sealing, anaerobic environment, high temperature and high pressure under solvothermal conditions[35–38]. Long-range crystalline order achieved by structural self-healing is primarily via reversible polymerization[19,39]. The insoluble and infusible nature of COFs makes the processing of crystalline COF powders into uniform films with the desired morphology very difficult. Surface-induced polymerization with reactive bromine side groups where the surface acts both as a template and a catalyst for Ullmann coupling of molecular precursors was used to deposit monolayer COF sheets of hundreds of nanometers in lateral size onto metal single crystals[40–42]. However, adjusting the film thickness and device fabrication by transferring them from these single-crystal metals to other substrates still remains a great challenge. The feasibility of the gas-liquid and liquid-liquid interface methods makes them employed at present, but they need complicated and skilled postsynthesis transfer process[43–46], which is neither suitable for large-area synthesis under ambient growth conditions, nor compatible with established patterning and integration methods. The possibility of polymerization reaction taking place in the substrate surfaces via solid-liquid interface has also been studied recently[27–29,47,48], and growth of the boronate ester-linked 2D COF films on device-relevant substrates without precipitate contamination was demonstrated via template colloidal approach[27]. The synthesis method is mostly based on the separation of templated-heterogeneous nucleation from the homogenous nucleation that occurred in the solution, and multiple equivalent polymerizations are employed to control the thickness. However, independent polymerization of organic precursors in solution has no impact on the film thickness except increasing the production cost.

Currently, most COF films are assembled via the one-step direct reaction between two types of precursors in liquid phase[39,49–54] by concurrent polymerization and crystallization, which are often accompanied by a loosely packed and less ordered structure. Adjusting the reaction rate and mode has been judged to be an elegant method for preparing highly crystalline imine COFs[37,38]. In these methods, high-quality crystallization is enabled by adding an aniline passivation agent, which ensures the self-healing of the framework under reversible conditions. It is also the case for the restricted growth of COF crystals, in which surfactant monolayers can promote the arrangement of the monomers[16], and the micelles formed by these amphiphilic molecules can regulate the polymerization and crystallization processes[55]. However, these research strategies were only used for COF powders. Here, we developed a diffusion-limited synthesis strategy to realize the preparation of uniform oriented COF films directly on substrates (Fig. 1a). The COF prepolymer/4,4′,4″,4‴-(1,3,6,8-Tetrakis(4-aminophenyl) pyrene (PyTTA) precursor/growth substrate sandwich structure not only limits the diffusion and reaction between the PyTTA films encapsulated in the system and the terephthalaldehyde (TPA) monomers dissolved in organic solution, but also regulates the orientation process of the predeposited PyTTA precursor film due to the penetration of solvent, which guides the formation of high-crystalline PyTTA-TPA COF films on its surface step by step. This approach is compatible with various molecular building blocks, and suitable for large-scale and pattern synthesis of COFs featured with high-crystalline quality, controllable thickness, low surface roughness and low production cost. Furthermore, it can be applied for the preparation of vertical heterojunctions by using 2D atomic crystals as substrates, thus enabling the fabrication of organic/inorganic hybrid film materials for electronic devices.

Results

Diffusion-limited synthesis method

The method for 2D COF films synthesized directly on substrates is based on the diffusion-limited Schiff base reaction between PyTTA and TPA (Fig. 1b). As shown in Fig. 1a, via thermal evaporation, a PyTTA film was firstly loaded on a growth substrate with a controllable thickness (Supplementary Figs. 1 and 2), which can also be patterned through a shadow mask. To confine the reaction of the PyTTA film on the substrate surface with TPA in organic solution, the film was firstly exposed to vaporized TPA molecules in a home-made pressure vessel, which generates a layer of PyTTA-TPA prepolymer coat on its upper and side surface (Supplementary Figs. 3–6). Subsequently the PyTTA-TPA prepolymer/PyTTA film/substrate system was immersed in a 1,2-dichloroethane ($C_2H_4Cl_2$) solution of TPA. Cross-linked PyTTA-TPA polymer is insoluble (Supplementary Figs. 7–9), thus the PyTTA-TPA prepolymer film, together with the growth substrate, separates the PyTTA precursor film in the system and TPA monomers in solution. $C_2H_4Cl_2$, acetic acid catalyst and TPA molecules can diffuse through the pores in the prepolymer film into the system (Supplementary Fig. 10), dissolve, regulate PyTTA monomers, and promote the reaction between PyTTA and TPA monomers (Supplementary Fig. 11). The reverse diffusion was inhibited due to the larger size of PyTTA precursors (Supplementary Fig. 10), indicating the feasibility of preparing COF films directly on substrate surfaces via diffusion-limited synthesis strategy. Grazing Incidence Wide Angle X-Ray Scattering (GIWAXS) indicated the PyTTA precursor film in the system-oriented along the surface of the crystalline substrate (Supplementary Figs. 12 and 13). And, UV-Vis absorption spectra indicated that the TPA precursors in solution were consumed with increasing reaction time (Supplementary Fig. 14). The diffusion amount of TPA into the system is affected by the thickness and pore size of prepolymer (Supplementary Figs. 15–18). Compared to the liquid phase reaction[56,57], the prepolymer slows down the reaction progress between PyTTA and TPA monomers, thus the obtained 2D PyTTA-TPA fragments have ample time to diffuse and self-heal along the surface of the oriented PyTTA film, forming a high-crystalline COF film in a step-by-step fashion (Supplementary Figs. 19 and 20). The solution-phase reaction is performed at room temperature, and the degree of reaction is related to the thickness of PyTTA films (Supplementary Figs. 21 and 22). After a 7-day reaction, the substrate changed colour from light green to yellow, suggesting the microstructure of the precursor film has changed (Fig. 1c).

There are mainly three main processes in the diffusion-limited film conversion method: precursor deposition, surface polymerization and diffusion-limited synthesis, which offer four key advantages. First, by selecting smooth growth substrates and controlling the evaporation rate of PyTTA, control of the morphology, size and thickness is achieved which is also suitable for industrial production. Second, during the diffusion-limited synthesis process, the PyTTA-TPA polymer coat is steady on the precursor surface. The reaction is confined in the system constructed by the COF prepolymer and growth substrate, thus avoiding disturbance and powder contamination. This is in contrast to the conventional interface synthesis[50,58–62], in which slight fluctuation of the liquid surface will result in the breakage of thin film floated at a gas-liquid or liquid-liquid interface, and in which a complex COF film will be formed with large surface roughness and even powder contamination via gradual deposition at the interface. Third, the PyTTA-TPA polymer layer can be finally crystallized into high-crystalline COFs, which do not contaminate the PyTTA-TPA COF film due to the same composition structure (Supplementary Fig. 23).

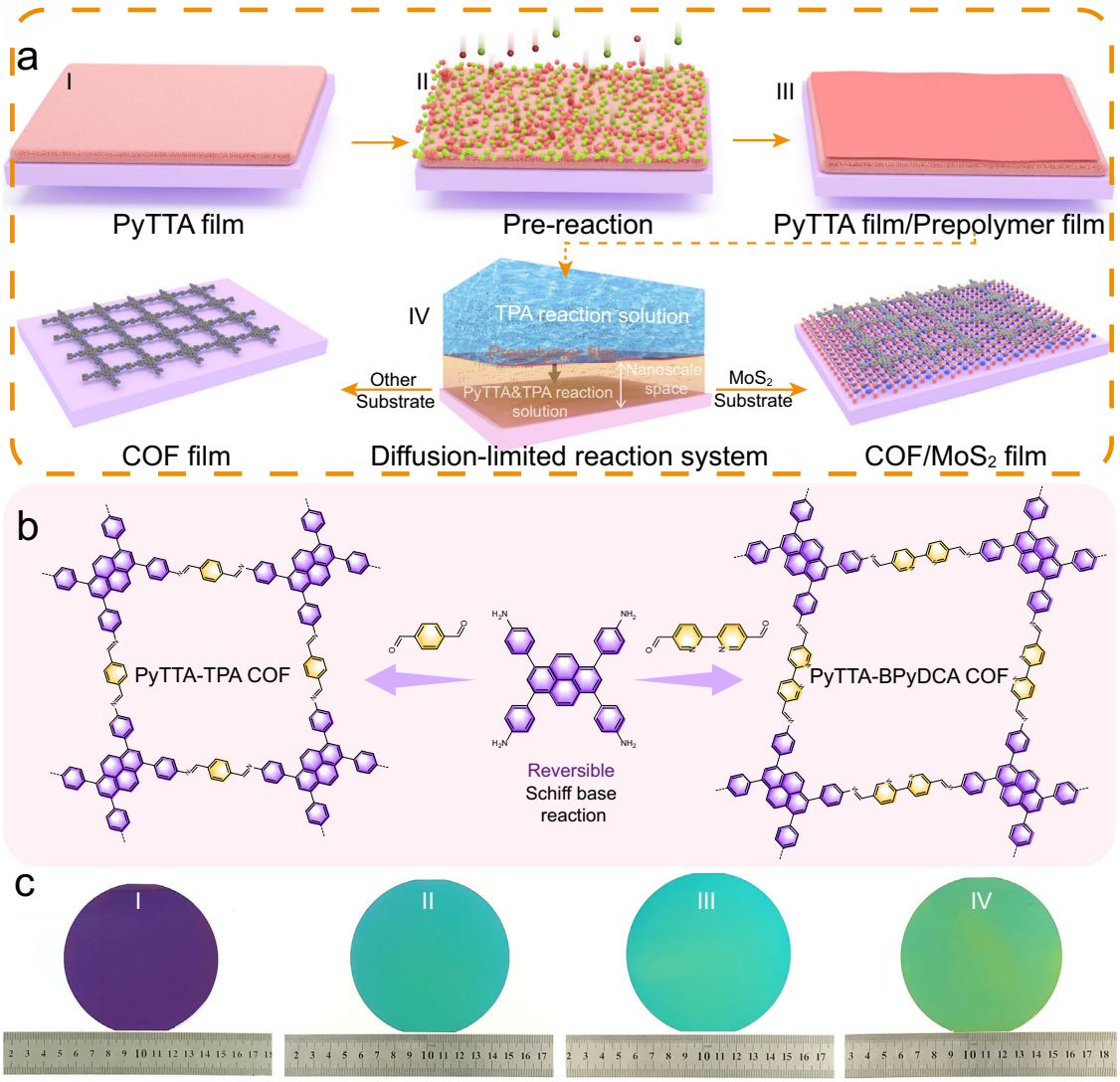

Fig. 1 | Diffusion-limited synthesis of 2D COF film. a Schematic illustration of the fabrication process of wafer-scale 2D COF films. **b** Schematic representation for the growth of imine-linked 2D COF films. **c** Photographs of SiO_2/Si substrate (I), PyTTA film (II), prepolymer film (III) and PyTTA -TPA COF film (IV).

Fourth, the PyTTA-TPA COF film orients along substrate surface, and high-crystalline oriented PyTTA-TPA COF film can be obtained on atomically flat substrates, e.g., MoS_2, graphene and sapphire (Fig. 2 and Supplementary Figs. 24–26). Additionally, the unreacted TPA precursors remaining independent in the solution during the synthesis process can be recycled. By avoiding specific reaction systems, the diffusion-limited synthesis makes the preparation much easier and thus becomes useful for the large-scale production of COF films at a lower cost.

Structural characterizations

Uniformity of the PyTTA-TPA COF films obtained by the diffusion-limited method was confirmed by optical images which showed a clear contrast with the substrate (Supplementary Fig. 27). Upon heating, or in the presence of TPA gas and organic solution, the surface remained clean, smooth and intact. Even after enlarging the image, no powder contamination was observed. Likewise, we used this strategy to achieve patterning of COF films in solution (Supplementary Fig. 28). To study its structure in detail, we cut the films and characterized their contour structure via an atomic force microscope (AFM). By controlling the thermal evaporation time, the thickness of obtained COF films was found to range from 23 to 209 nm. Detailed measurements indicated a statistically linear correlation between the thickness of PyTTA and PyTTA-TPA COF films (Supplementary Figs. 2, 29 and 30). We observed all the resultant COF films do have smooth surfaces which are inconsistent with the reported nucleation and growth of COF films at the interface[50–52], where the surface roughness is increased with the sedimentation of nanoparticles (Supplementary Fig. 31).

The chemical structure of PyTTA-TPA COF films is characterized by employing Fourier transform infrared spectroscopy (FT-IR), Raman and X-ray photoelectron spectroscopy (XPS). Similar to that of PyTTA powder, peaks at ~3334 and 3231 cm^{-1} are due to the vibration bands of the NH_2 group of PyTTA molecules. After polymerization, peak at ~1701 cm^{-1} appeared due to the C=O unit of TPA, and the characteristic bands at 1624 cm^{-1} in the FT-IR spectra indicated the formation of imine linkages[63] (Fig. 2a). Similar results are also obtained by Raman spectra (Fig. 2b), where the formation of a uniform COF film (Fig. 2c) was confirmed by spatial dependence of the characteristic Raman peak intensity (~1576 cm^{-1}). In addition, according to the XPS spectra of PyTTA-TPA COFs (Supplementary Fig. 32), the high-resolution N 1 s signal consists of two peaks located at around 399.4 eV and 398.9 eV, corresponding to the unreacted NH_2 groups and the C=N bond structure, respectively, which also confirms the chemical structure of PyTTA-TPA COF.

We have explored the relationship between crystal structure and synthesis time via Grazing Incidence X-ray Diffraction (GIXRD)

https://doi.org/10.1038/s41467-024-54844-4

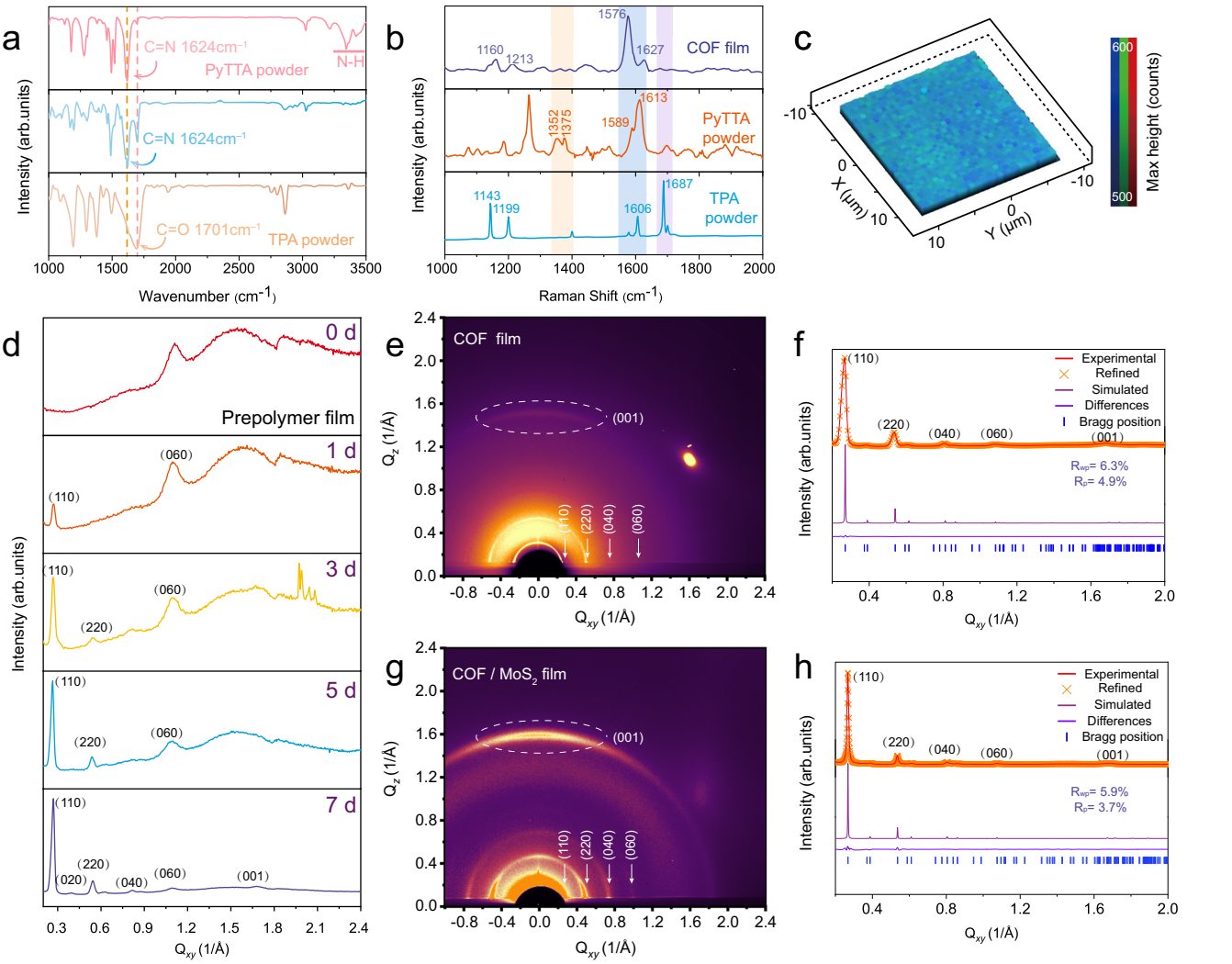

Fig. 2 | Spectral characterizations of PyTTA-TPA COF films. a FT-IR spectra of PyTTA, TPA and PyTTA-TPA COF film. **b** Raman spectra of PyTTA, TPA and PyTTA-TPA COF film. **c** Raman spectroscopy map of the peak at ~1576 cm^{-1}. **d** GIXRD spectra of PyTTA-TPA COF films at different reaction times. **e** GIXRD image of PyTTA-TPA COF film prepared on SiO_2/Si substrate. **f** In-plane GIXRD profiles of the COF film. **g** GIXRD image of PyTTA-TPA COF/MoS_2 hybrid film. **h** In-plane GIXRD profiles of the PyTTA-TPA COF/MoS_2 hybrid film.

(Fig. 2d). The GIXRD spectrum of the PyTTA-TPA prepolymer film shows strong peaks located at q = ~1.1 $Å^{-1}$ and 1.6 $Å^{-1}$, but no diffraction peak of PyTTA-TPA COFs. However, immersing the film in dichloroethane solution of TPA for 1 day showed the appearance of the signal corresponding to the (110) plane of PyTTA-TPA COF, and a square lattice is observed in some small domains (Supplementary Fig. 20). The extent of crystallinity was enhanced with increasing time as observed from the change of (110) peak, and at the molecular level, crystal domains stick closely in the film (Supplementary Fig. 20). In addition, the thickness of the PyTTA films also affected the reaction time. The thicker the PyTTA film, the longer the reaction time. We obtained a maximum thickness of about 209 nm for the PyTTA-TPA COF films in our experiments.

The sample of a PyTTA-TPA COF film after 7-day reaction showed a strong (110) peak located at q = ~0.27 $Å^{-1}$ (Fig. 2e, f). In addition, three prominent diffraction peaks were also observed at ~0.54, 0.81, 1.68 $Å^{-1}$, which can be assigned to the (220), (040), and (001) facets, respectively (Fig. 2f). Such features coincided with the simulated XRD pattern in an AA eclipse stacking mode (Supplementary Table 1). The grain domain size in the PyTTA-TPA COF film was obtained to be ~75.7 nm as calculated by Scherrer's analysis and was comparable to that of the PyTTA-TPA COF powders (~57.5 nm) (Supplementary Fig. 33). The periodicities in the (110) plane is indicated by high intensity of the peak at 0.27 $Å^{-1}$ and is also suggestive of a well-defined ordered columnar array. The peak at ~1.68 $Å^{-1}$ corresponding to the (001) plane is associated with the interlayer distance, and its presence is indicative of good stacking order. From the chart (Fig. 2e and Supplementary Fig. 26), the in-plane and out-of-plane XRD profiles show a drastic change in the intensity of (001) peak, proving the formation of preferentially oriented COF films that preferably lie with the ab plane parallel to the smooth SiO_2/Si substrate surface. Under identical experimental conditions, the induced orientation effect of the growth substrate on the growth of COF was verified by using MoS_2 films as the growth substrate (Supplementary Figs. 34–40). As shown in Fig. 2g, the GIXRD pattern showed enhanced signals due to higher crystalline quality. Besides, the peaks corresponding to (110), (220), (040) and (001) planes of the PyTTA-TPA COF are observed (Fig. 2g, h), the full width at half-maximum (FWHM) of the (110) peak for the PyTTA-TPA COF/MoS_2 hybrid film was 0.022 $Å^{-1}$, along with improved grain size of ~160.7 nm. Therefore, the selection of an atomic smooth surface as the growth substrate is important for the synthesis of highly crystalline COF films.

https://doi.org/10.1038/s41467-024-54844-4

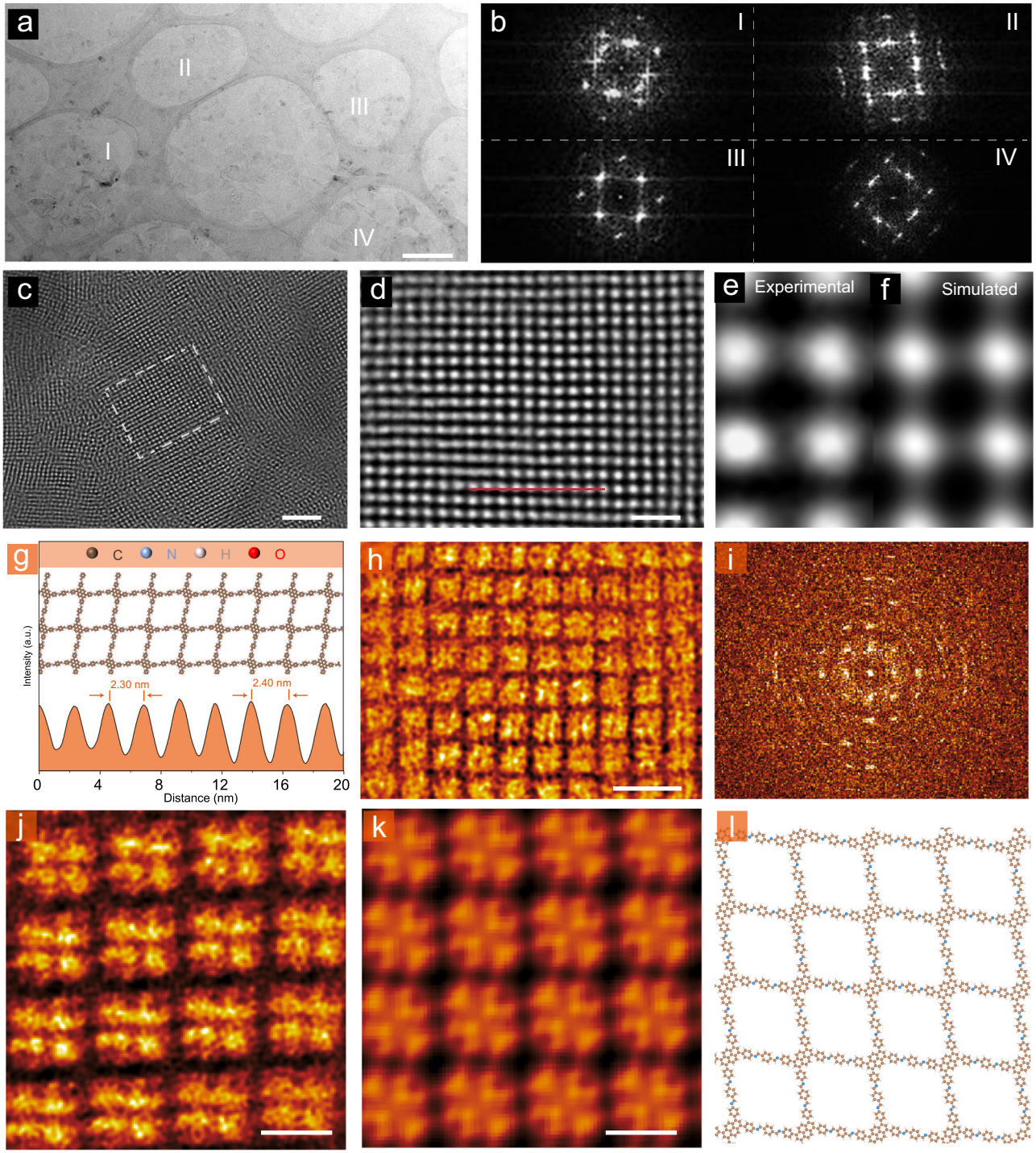

Fig. 3 | TEM characterizations of PyTTA-TPA COF films. a Low-magnification TEM image of PyTTA-TPA COF film with a thickness of ~20 nm on a copper grid. Scale bar 500 nm. **b** Corresponding FFT images from the areas labeled in **a**. **c**, **d** TEM images of the PyTTA-TPA COF film with different magnifications. Scale bar 20 nm in **c**, 10 nm in **d**. **e**, **f** Experimental (**e**) and simulated (**f**) TEM images of PyTTA-TPA COF. **g** Intensity profiles acquired along the red line in **d**. **h** Low-dose TEM image of PyTTA-TPA COF film. Scale bar 5 nm. **i** Corresponding FFT image from the region in **i**. **j**–**l** Low-dose TEM image of PyTTA-TPA COF film (**j**), the corresponding simulated image (**k**) and atomic model (**l**). Scale bar 2 nm in **j** and **k**.

The PyTTA-TPA COF films synthesized via the diffusion-limited method can be transferred onto a Cu grid after stripping from growth substrates for transmission electron microscopy (TEM) characterizations (Fig. 3a). The corresponding fast Fourier Transform (FFT) patterns of four locations in the thin film display sharp diffraction spots with square pattern, indicating its high crystallinity (Fig. 3a, b). The different crystallographic orientations (Fig. 3b) in the four regions reveal the polycrystallinity of the film. From the high-magnification TEM image (Fig. 3c and 3d), the PyTTA-TPA COF film shows periodic ordering and an almost orthogonal lattice arrangement. Based on HRTEM image simulations, the bright points correspond to the pores between the pyrene units (Fig. 3e, f). The intensity profile acquired along the red line (in Fig. 3d) is shown in Fig. 3g. Separation between the neighboring framework (black contrast), and pore (bright

https://doi.org/10.1038/s41467-024-54844-4

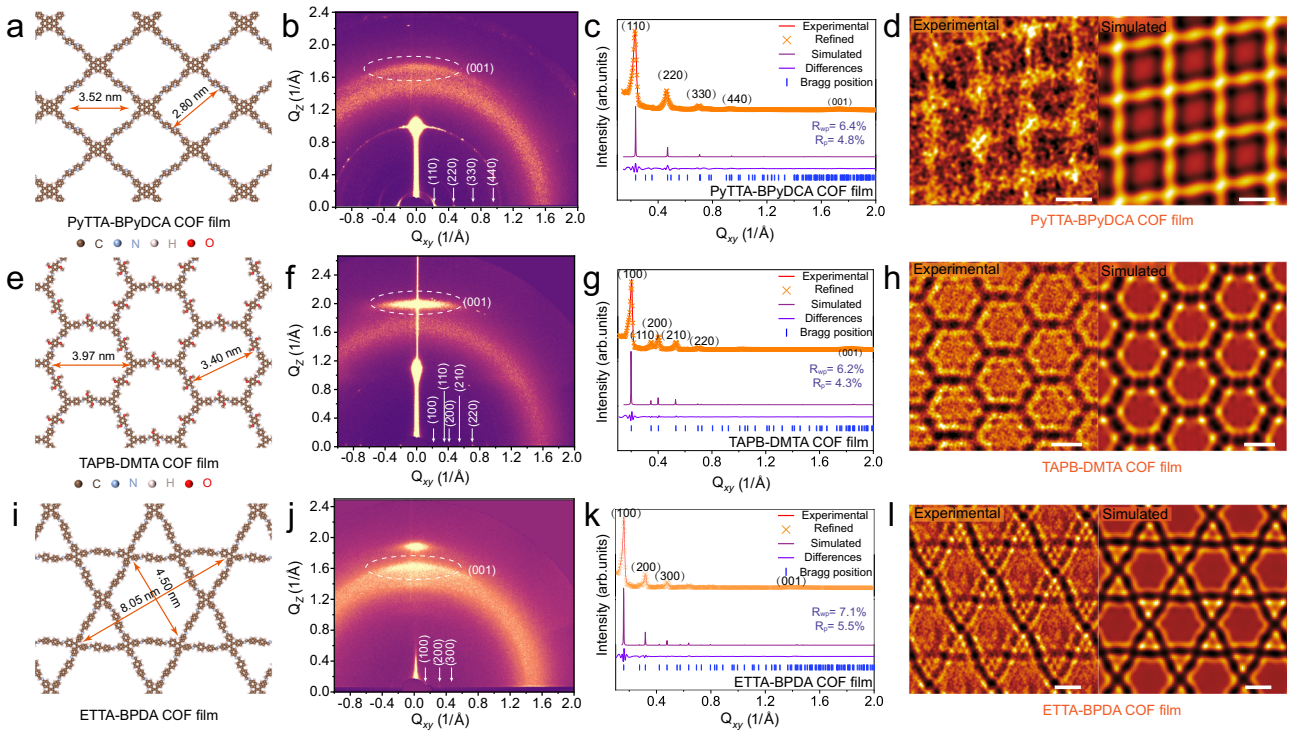

Fig. 4 | GIXRD and STEM characterizations of COF films. a Simulated molecular structure of PyTTA-BPyDCA COF. **b**, **c** GIXRD image and in-plane GIXRD profiles of PyTTA-BPyDCA COF/MoS_2 hybrid film. **d** Experimental (left) and simulated (right) low-dose TEM images of PyTTA-BPyDCA COF film. Scale bar 2 nm. **e** Simulated molecular structure of TAPB-DMTA COF. **f**, **g** GIXRD image and in-plane GIXRD profiles of TAPB-DMTA COF/MoS_2 hybrid film. **h** Experimental (left) and simulated (right) low-dose TEM images of TAPB-DMTA COF film. Scale bar 2 nm. **i** Simulated molecular structure of ETTA-BPDA COF film. **j**, **k** GIXRD image and in-plane GIXRD profiles of ETTA-BPDA COF/MoS_2 hybrid film. **l** Experimental (left) and simulated (right) low-dose TEM images of ETTA-BPDA COF film. Scale bar 2 nm.

contrast) sites are ~2.4 nm, which is consistent with the calculated lattice constant of PyTTA-TPA COFs, agreeing with the AA-stacked atomic models of PyTTA-TPA COF sheet layers. We then visualized the molecular structure of PyTTA-TPA COFs via low-dose high-resolution imaging, which showed a nearly square lattice arrangement with a 2.4 nm interplanar spacing (Fig. 3h) verified by the corresponding FFT pattern (Fig. 3i). The molecular scaled low-dose image shows the ordered arrangement of bridging pyrene and knots units in the COF lattice (Fig. 3j), as marked by a black mesh, which was verified by the simulated image (Fig. 3k) from density functional theory (DFT) optimized model (Fig. 3l).

The diffusion-limited synthesis method is not limited to PyTTA-TPA COF film. Based on the topology design principle, a variety of configurations of COF films were also fabricated on SiO_2/Si and MoS_2 substrates including C_4-C_2-structural PyTTA-BPyDCA, C_3-C_2-structural TAPB-DMTA and D_{2h}-C_2-structural ETTA-BPDA COF films (Fig. 4 and Supplementary Figs. 41–45) using TAPB (1,3,5-Tris(4-aminophenyl) benzene), ETTA (Tetrakis(4-aminophenyl)ethene), BPyDCA ([2,2′-Bipyridine]−5,5′-dicarbox-aldehyde), DMTA (2,5-Dimethoxyterephthalaldehyde) or BPDA ([1,1′-Biphenyl]−4,4′-dicarbaldehyde) instead of PyTTA, TPA as precursors. These COF films also showed an orientation on MoS_2 substrates according to the in-plane and out-of-plane signals of the (001) peaks (Fig. 4b, f, j). All the COF films showed an AA-stacked atomic model (Supplementary Tables 2–4) based on the Pawley refinement results (Fig. 4c, g, k). The unit cell parameters of PyTTA-BPyDCA COF belonging to the C2/m space group were $a = 4.26$ nm, $b = 3.68$ nm, $c = 0.4$ nm, $\alpha = 90°$, $\beta = 90.5°$, and $\gamma = 90°$. For the TAPB-DMTA COF belonging to the P6 space group, the unit cell parameters were $a = 3.68$ nm, $b = 3.68$ nm, $c = 0.35$ nm, $\alpha = 90°$, $\beta = 91°$, and $\gamma = 120°$ while unit cell parameters were $a = 4.65$ nm, $b = 4.65$ nm, $c = 0.45$ nm, $\alpha = 90°$, $\beta = 90°$, and $\gamma = 120°$ for the ETTA-BPDA COF belonging to the P6 space group. The TEM images of all three COF films clearly present orderly crystalline structures (Supplementary Fig. 46). There are almost no significant amorphous regions that are observed between the crystal regions and grain domains get together side by side, indicating the high-crystalline quality of the obtained COF films. However, these three COF films have different framework structures, as demonstrated by the HRTEM images and the corresponding FFT patterns. For further investigating the crystalline phase and microstructure within PyTTA-BPyDCA, TAPB-DMTA and ETTA-BPDA COF film, we carried out low-dose molecular scaled characterization. The high-resolution low-dose TEM images show obvious framework features with lattice constants of ~2.8 nm, ~3.4 nm, and ~4.5 nm (Fig. 4d, h and Supplementary Fig. 42), consistent with the calculated models (Fig. 4a, e, i), respectively. As shown in Fig. 4d, h and Supplementary Fig. 42, PyTTA-BPyDCA COFs have orthogonal features, and TAPB-DMTA COFs have hexagonal features, while ETTA-BPDA COFs have Kagome features. These results are in agreement with the calculated structures of PyTTA-BPyDCA, TAPB-DMTA and ETTA-BPDA COF films by GIXRD.

Theoretical calculation

The crystalline quality of the oriented 2D COF films is higher than those prepared via vapor-solid interface conversation by the concurrent polymerization and crystallization during film formation[39,50,51]. To reveal the underlying mechanism, extensive multi-scale calculations were performed (Fig. 5 and methods for calculation details). Due to the planar structure of PyTTA molecules and the atomically smooth surface of MoS_2, the first PyTTA molecular layer deposited on MoS_2 surface would preferentially show a planar alignment induced by the vdW interaction between MoS_2 and PyTTA. Such a planar configuration of the first PyTTA molecular layer will further act as a template for the

https://doi.org/10.1038/s41467-024-54844-4

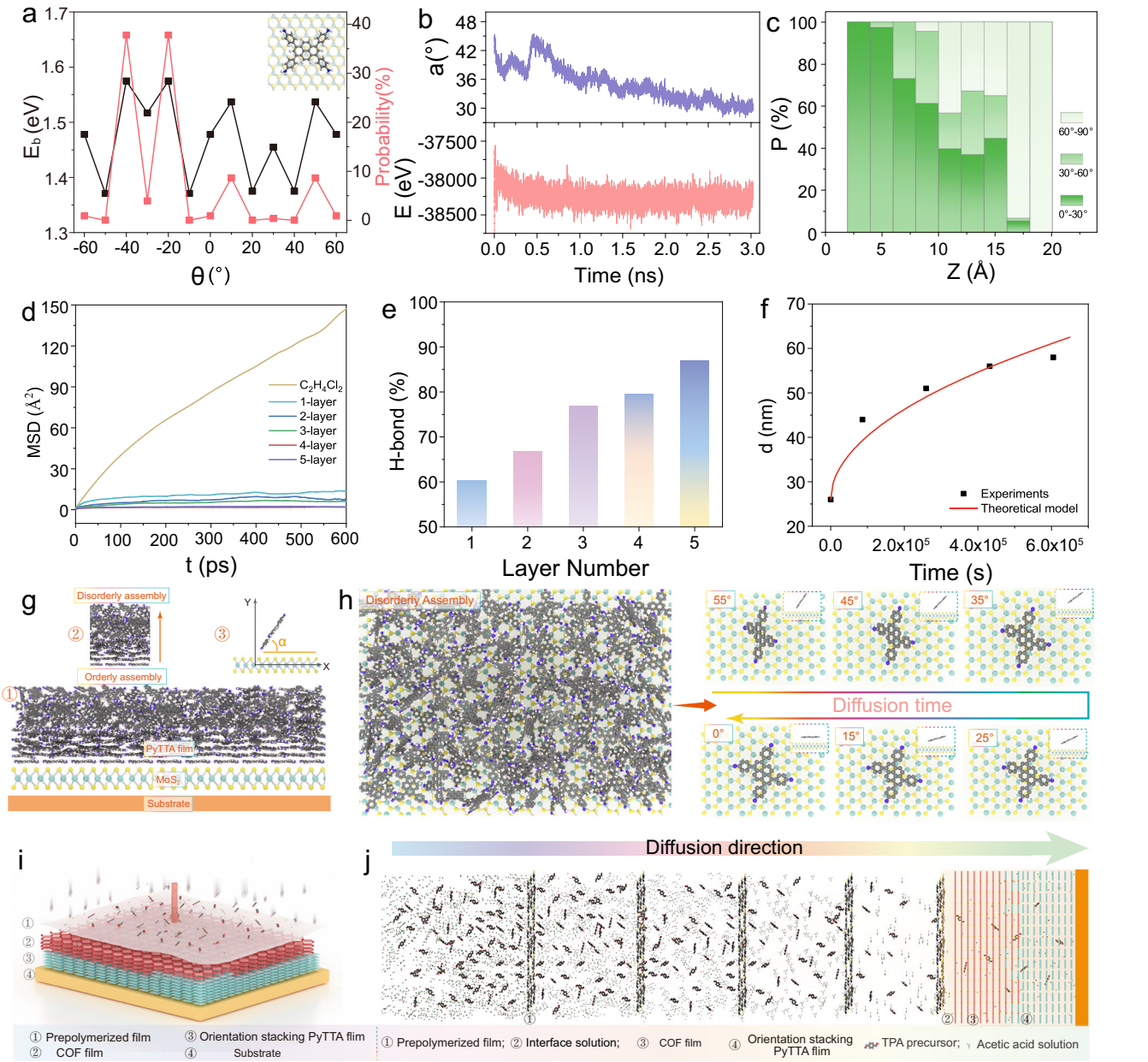

Fig. 5 | Theoretical calculation of the mechanism and chemical kinetics. a The binding energy E_b and in-plane orientation probability profiles of a PyTTA on the basal plane of MoS_2. **b** The average angle (α) profile (upper panel) between the PyTTA molecular plane and the MoS_2 basal plane and the system total energy profile (lower panel) during MD simulation. **c** Spatial distribution probability of the angle between PyTTA molecules and the MoS_2 plane during the last 0.15 ns MD simulation in **b**. **d** Molecular simulations on MSD of TPA diffusion in pure $C_2H_4Cl_2$ solution and in $C_2H_4Cl_2$ solution with different layers of PyTTA-TPA COFs. **e** Statistical data of oxygen atoms forming hydrogen bonds in MD simulations in **d**. **f** The variation of COF film thickness with synthesis time. **g** Schematic of PyTTA film assembly by thermal vaporization on MoS_2 surface. **h** Schematic representation of the molecular transition of disordered assembled PyTTA after immersion in $C_2H_4Cl_2$ solution. **i** Schematic representation of the reaction of self-assembled PyTTA in the reaction solution. **j** Schematic diagram of the kinetic growth model of high-quality COF based on hydrogen bond-limited diffusion.

alignment of subsequently deposited PyTTA molecules. Besides, we found that the first PyTTA molecular layer also shows a preferential in-plane orientation. Figure 5a shows the binding energy E_b profile of a PyTTA on the basal plane of MoS_2 as a function of their relative in-plane orientation θ, as obtained by DFT calculations. It can be seen that $E_b(\theta)$ changes from 1.37 to 1.58 eV ($-60° \le \theta < 60°$ due to the D_{3h} symmetry of MoS_2), with the maxima located at θ around $-40° \le \theta < -20°$. The relatively large binding energy difference (~0.2 eV) as compared to thermal fluctuation at the experimental temperature of 300 K (k_BT= 0.026 eV, where k_B and T are the Boltzmann constant and temperature, respectively) will further lead to a preferential in-plane orientation arrangement of PyTTA molecules on MoS_2 surface (Supplementary Figs. 47 and 48). As shown in the in-plane orientation distribution profile calculated by $\frac{e^{E_b(\theta_i)/k_BT}}{\sum_i e^{E_b(\theta_i)/k_BT}}$ (Fig. 5a), ~80% of PyTTA molecules show their orientations within $-40° \le \theta < -20°$. DFT calculations also showed that the diffusion of PyTTA on MoS_2 surface is ultrafast, with the diffusion time of PyTTA on MoS_2 by one crystal lattice to be only ~1.2 ns at room temperature (See SI for calculations, Supplementary Fig. 47). Given the strong and anisotropic binding as

https://doi.org/10.1038/s41467-024-54844-4

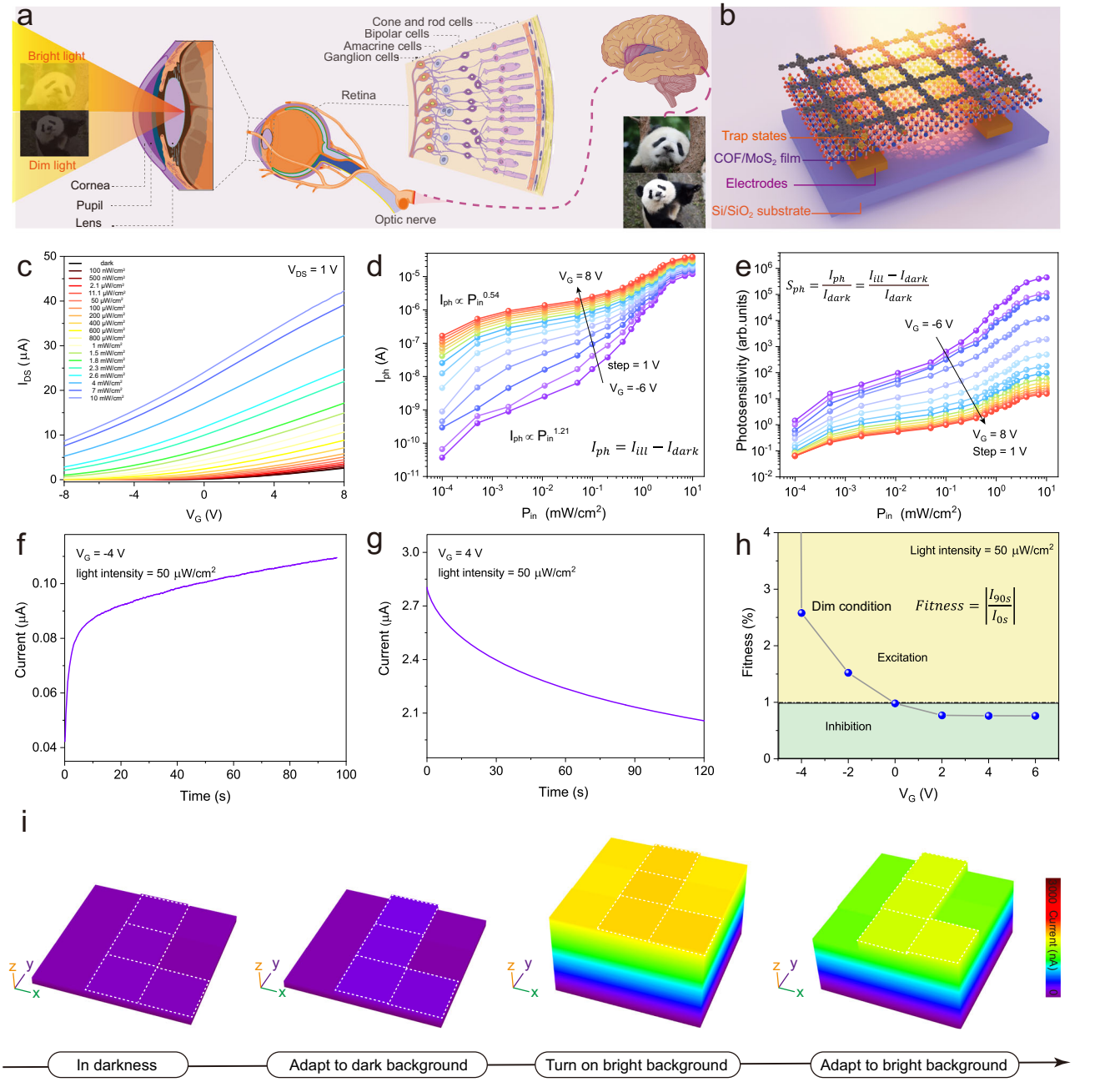

Fig. 6 | Photosensitive characteristics of PyTTA-TPA/COF/MoS_2-based phototransistors. a Schematic diagram of the dynamic regulation process of human visual adaptation. **b** Schematic of the phototransistors. **c** Transfer characteristic curves of the phototransistor carried out at $V_D = 1$ V under various P_{in} values (460 nm wavelength). **d** The function between I_{ph} and P_{in} for the condition of different V_G values. **e** S_{ph} is a function of P_{in} under different V_G values. **f**, **g** Real-time current response of the phototransistor at V_G values of −4 V (**f**) and +4 V (**g**). **h** Extracted current fitness at various V_G values. **i** Results of current mapping of device array (3 × 3 light-sensing array) under different environmental conditions. A square corresponds to a device. The size of a device is 1000 μm × 300 μm. In the dark or bright constant stimulus light background, the L-shaped image contrast displays and gradually actively adapts the achieved spatially resolved discrimination.

well as the ultrafast diffusion of PyTTA on MoS_2, PyTTA molecules can quickly form a highly orientated molecular layer on MoS_2 surface in the early deposition stage, which will template the alignment of subsequently deposited PyTTA molecules[64].

However, further deposition leads to randomly oriented PyTTA molecules on the as-formed highly oriented PyTTA monolayer due to the weak interaction between PyTTA molecules and fast deposition rate, leading to the formation of an amorphous PyTTA thin film in our experiments (Fig. 5g), as shown in our GIWAXS data (Supplementary Fig. 12). More importantly, we found that after sunk in the $C_2H_4Cl_2$ solution the PyTTA molecules in such an amorphous thin film will become highly oriented on MoS_2 substrate due to π-π vdW interaction between pyrene backbones of PyTTA molecules (Supplementary Fig. 13). To elucidate this phenomenon, molecular dynamics (MD) simulations were performed (Supplementary Fig. 49). As shown in Fig. 5b, the average angle (α) between PyTTA molecule planes and the MoS_2 basal plane quickly decreases from 45° to 30° within 3 ns after the PyTTA film merged in $C_2H_4Cl_2$ solution, which is accompanied by the continuous decrease of system total energy. Moreover, the spatial distribution α along the perpendicular direction of the MoS_2 basal

plane shows that PyTTA molecules closer to the MoS_2 surface (or the preformed highly oriented PyTTA monolayer) will first become parallel to the MoS_2 surface, which further guides the rearrangement of PyTTA molecules away from the MoS_2 surface (Fig. 5c, g, h), Limited by the size of the simulation system and simulation period, the thickness of PyTTA film where a planar alignment can extend is difficult to be determined. In our experiments, the thickness of the PyTTA molecular thin film that was found to show a highly planar molecule alignment is 120 nm, suggesting the long-range templating effect of the first PyTTA molecular layer on MoS_2. To investigate the effect of the oriented PyTTA film on the growth of COF films, PyTTA crystals were prepared by recrystallization and used as a template for PyTTA-TPA COF synthesis. The results show that the COFs on PyTTA crystal surface have high crystal quality (Supplementary Fig. 50). Therefore, we think that the highly orientated configuration of PyTTA film guides the nucleation and growth of high-crystalline COF film on its surface. It is worth mentioning that a very recent study has employed the preferentially planar alignment of precursor molecules on substrates to synthesize highly crystalline MOF thin films[65].

We further established a diffusion-limited growth model for the synthesis of a high-quality COF film, where the diffusion of TPA across the formed PyTTA-TPA atomic layers governs the growth of the COF film. To simplify calculations, we used complete COF layers instead of prepolymer coating. As shown in Fig. 5d, we calculated the mean square displacement (MSD) of TPA in both pure $C_2H_4Cl_2$ solution and systems of $C_2H_4Cl_2$ solution with different numbers of COF atomic layers by MD simulations. The diffusion coefficient of TPA in pure $C_2H_4Cl_2$ solution (~3.65×10^8 nm^2/s) can be obtained by linear fitting of the MSD curve as a function of time, which is close to the experimentally measured self-diffusion coefficient of $C_2H_4Cl_2$ (~10^9 nm^2/s)[66]. Strikingly, the diffusion coefficient of TPA across 1 COF atomic layer (1.42×10^7 nm^2/s) is one order of magnitude lower than that in pure $C_2H_4Cl_2$ solution. When the number of COF layers is increased to 2 and 3, the diffusion coefficient of TPA molecules decreases to 6.41×10^6 nm^2/s and 5.78×10^6 nm^2/s, respectively. It becomes almost immobile if the COF layer number further increases to 4, suggesting the relatively strong interaction between TPA and COF (Fig. 5d, j and Supplementary Fig. 51). A closer inspection of the MD simulation trajectories shows that hydrogen bonds are formed between the oxygen atoms in TPA and hydrogen atoms in COF. Figure 5e shows the statistics of the proportion of oxygen atoms that form hydrogen bonds in MD simulations. It can be seen that the proportion of oxygen atoms in TPA to form hydrogen bonds increases from 60.3% to 86.8% with the increase of COF atomic layer number from 1 to 4, which well explains the ultra-low diffusion of TPA across COF layers. Because diffusion of TPA molecules across COF films requires repetitively breaking and forming hydrogen bonds between them, the hydrogen bonding strength (0.54–0.65 eV, depending on adsorption position) between TPA and COF is calculated by DFT, and the diffusion coefficient of TPA across COF films with layer number ≥4 is estimated to be only $2.18–1.51 \times 10^2$ nm^2/s (See Supplementary Figs. 51 and 52 for calculation details). Based on the above calculations, we proposed a diffusion-limited growth model for the COF film (Fig. 5i, j). Considering the ultra-low diffusion of TPA across COF atomic layers, TPA molecules from the $C_2H_4Cl_2$ solution to the bottom PyTTA layer will be totally consumed by PyTTA to form new COF layers. Therefore, the growth rate of COF layers is proportional to the diffusion flux of TPA:

$$\frac{d\delta}{dt} = \alpha D \nabla c = \alpha D \frac{c}{\delta}, \quad (1)$$

where δ is the thickness of the growing COF film, t is time, $\alpha = \frac{\lambda}{\rho}$ with λ to be the interlayer distance between COF atomic layers (0.34 nm) and ρ is the area concentration of the TPA linker in one COF layer (0.32 nm^{-2}), D is the diffusion coefficient of TPA across COF layers and c is the concentration of TPA in $C_2H_4Cl_2$ solution. Here, we employed a constant D, which is reasonable because the thickness of COF films synthesized in our experiments is tens of nm. From Eq. (1), we get $\delta(t) = \sqrt{\frac{2\lambda D c t}{\rho}}$. To verify our model, the thickness of COF films with the change of synthesis time was measured (Fig. 5f, See Supplementary Fig. 16 for experimental details), which is well consistent with our proposed model. Moreover, the diffusion coefficient of TPA is extracted to be 1.09 nm^2/s, which is quite close to our DFT estimation and further validates the limited growth model.

Adaptive visual function

The visual adaptative functions of the human visual system can enable organisms to achieve the dynamic balance of visual information in constantly changing conditions (Fig. 6a). According to physiological studies, the iris can control the size of the pupil by contracting and relaxing the sphincter muscle, thereby altering the light entering the eye and playing a regulatory role in adapting to complex lighting environments. Further analysis at the cellular level showed that in the cell membrane, the time-dependent adjustment of ion channel gating is contributed by the human visual adaptation which is to achieve the dynamic balance of the visual information in dim or high light conditions[67]. Human visual adaptation can be ideally simulated in low-dimensional vdW heterostructure[68]. And 2D COF materials have been proven to have high chemical stability, (Supplementary Figs. 53 and 54), excellent optical performance and biocompatibility[69,70]. Therefore, we fabricated phototransistors using PyTTA-TPA COF/MoS_2 vertical hybrid materials as active layers (Fig. 6b), which resulted in efficient optical absorption by allowing direct illumination onto the surface of COF film (Supplementary Figs. 55 and 56), when the MoS_2 film act as a conductive channel during the adaptive process (Supplementary Fig. 57). In addition, O_2-plasma treatment was used to introduce a large variety of localized trapping states, including donor-type and acceptor-type traps into the interface[71–73] (See Method and Supplementary Figs. 58–60). The existence of localized trapping states at the heterointerface between COF and MoS_2 allows to achievement visual adaptive process under various illuminations (Supplementary Fig. 61).

We have measured the optoelectronic performance of the PyTTA-TPA COF/MoS_2-based phototransistor under 400-nm light stimulation. Figure 6c shows the transfer characteristic curves of the phototransistor at a source-drain voltage (V_{DS}) of 1 V. With increasing illumination (P_{in}) from 100 nW/cm^2 to 10 mW/cm^2, the rise of source-drain current (I_{DS}) takes place and the threshold voltages shift towards left, which is suggestive of increasing current density inside the conductive channel. Photocurrent (I_{ph}) and photosensitivity (S_{ph}) are both key parameters to illustrate the photoelectric performance of devices. The difference of I_{DS} under illumination and dark conditions is called as I_{ph} (Fig. 6d). Its near linear increase with P_{in} ($\alpha \approx 1.21$) at negative gate bias ($V_G = -6$ V) suggests photoconductive effect can be mainly attributed to the increase of photogenerated carrier density. However, increasing V_G makes the relation between I_{ph} and P_{in} sublinear, e.g., $\alpha \approx 0.54$ at $V_G = 8$ V. This is indicative of the change in domain adaptive mechanism to the photogating effect related to the trap states at the heterointerface. Therefore, it is possible to adapt to different illumination conditions by controlling the V_G via modulation of the mechanism of photocurrent generation. Figure 6e shows the relationship between S_{ph} and P_{in} under various V_G. The S_{ph} is negatively correlated to V_G: when the applied V_G is negative, the device shows high S_{ph}, whereas under positive V_G, S_{ph} of the device is low.

To further study the effect of V_G on controlling the adaptive process of the device, we explored the change in time-dependent current under continuous illumination of 50 μW/cm^2 (Fig. 6f, g). Fixing the V_G at −4 V resulted in a gradual increase of the I_{DS} over time (Fig. 6f), indicating the photoconductive effect causing an electron excitation process. In contrast, fixing the V_G at +4 V resulted in a

gradual decrease of I_{DS} with the extension of illumination time (Fig. 6g). For quantitative description of the device's photo-adaptive characteristics under different V_G, we defined the degree of current excitation and inhibition effect by using the relative change of I_{DS} at the 90 s to the maximum current (See Fig. 6h); the ratio is greater than 1 when V_G is more negative, indicating an enhanced excitation effect. Instead, when V_G is more positive, the ratio is smaller than 1 which is representative of an enhanced inhibition effect. Therefore, the device can realize the photo-adaptative function under changing conditions via controlling V_G. The adaptive process of the device from dim conditions to bright illuminate conditions is represented in Supplementary Figs. 62 and 63. Under dim conditions (<2.1 μW/cm^2), negative V_G was applied to realize the electron excitation process, while under bright conditions (800 μW/cm^2) positive V_G was applied to realize the inhibition process. Specifically, when P_{in} was 100 nW/cm^2 and 2.1 μW/cm^2, the ratio was 244% and 209% at the V_G of −4 V and −2 V, respectively. In sharp contrast, for V_G of 2 V, 4 V and 8 V, the P_{in} was 800 μW/cm^2, 2.3 mW/cm^2 and 10 mW/cm^2, and the respective ratio was 87%, 85%, and 83%. Unlike structure-induced optical modulation[5], the process is an active light adaptation behavior. V_G can be used to regulate photosensitive characteristics of the device, which is similar to an ion channel gating in the cell membrane under different light illumination conditions. Due to the wide absorption spectrum of PyTTA-TPA-COF/MoS_2 film, the device also exhibits excellent adaptability to red, green, and yellow light (Supplementary Fig. 64). Figure 6i shows the distribution of responses of the pixel spots in the sensing array under different environments. We were able to show L-shaped images of current distribution when different intensities of stimulus light were turned on in a dark background. When a strong light background was switched on instantaneously, the resolution of the L-shaped current distribution was impeded, and with continued stimulation, the L-shape gradually appeared. The results indicated that constructing a large-scale PyTTA-TPA/COF/MoS_2-based device array would have application potential for active light adaptation imaging, which is similar to the adaptative functions of the human visual system.

Discussion

In summary, we have developed a low-cost, general diffusion-limited method to directly synthesize high-crystalline 2D PyTTA-TPA COF films on substrates. Unlike the vapor-solid process with concurrent polymerization and crystallization, the method regulates the polymerization and crystallization processes on the substrate surface by controlling the orientation of PyTTA molecules and the diffusion of TPA monomers. The surface of the COF films is smooth with controlled thickness. The PyTTA-TPA COF film grown on MoS_2 film is highly crystalline and oriented, as has been confirmed by TEM and GIXRD. The method can also be used to prepare crystalline PyTTA-BPyDCA, TAPB-DMTA and ETTA-BPDA COF films, suggesting the general applicability of this method. Using the PyTTA-TPA COF/MoS_2 hybrid material film as active material, the obtained phototransistors display enhanced photoelectric performance, which can simulate the adaptative function of the human visual system. This work contributes to the industrialized preparation of oriented 2D COF films and their applications in interactive artificial intelligence, which is of great significance for basic research and practical applications.

Methods

Preparation of precursor film

PyTTA film was deposited on the growth substrate by a thermal evaporation method. A quartz crucible containing 20 mg of PyTTA (CHEMSOON Co., Ltd, China. Purity of 99%) powders as precursors was put in the hot evaporation chamber, and the growth substrate was loaded with its face down to the evaporation source. When the vacuum reached 6×10^{-6} mbar, PyTTA powders were gradually heated to 180 °C, and the evaporation rate of PyTTA was controlled at 0.1 Å/s to deposit PyTTA film on a growth substrate. The film thickness can be controlled by deposition time. Similarly, TAPB (CHEMSOON Co., Ltd, China. Purity of 99%) and ETTA (CHEMSOON Co., Ltd, China. Purity of 99%) precursor films were prepared at 140 °C and 170 °C, respectively.

Synthesis of COF film

In a glove box, the growth substrate with a PyTTA film on its surface was placed in a home-made container, and 30 mg of the precursor TPA (CHEMSOON Co., Ltd, China. Purity of 99%) and 100 μl of acetic acid catalyst were added to the reaction system (CONCORD TECHNOLOGY Co., Ltd, China. Purity of Analytical Reagent). The container was sealed and heated to 140 °C for a 6 h gas/solid reaction, and then the growth substrate was immersed into a 150 ml dichloroethane solution of TPA containing 1 ml acetic acid and 30 mg TPA dichloroethane. The reaction was kept for 1 week at room temperature. The growth substrate was purified, with dichloroethane as a solvent, by Soxhlet extraction (2 days). Finally, vacuum drying was carried out at 90 °C for 12 h to obtain COF film.

Characterizations of COF film

NIKON Eclipse LV-100 optical microscopy is used to characterize the morphology of the samples. Raman spectra were recorded using a Renishaw inVia Raman Microscope with laser excitation at 532 nm, and mappings were taken over an extended range (800–2500 cm^{-1}) with an exposure time of 10 s. Conventional TEM was performed with a JEM-2100 transmission electron microscope operated at a voltage of 200 kV. Low-dose TEM imaging was performed on FEI Titan Cubed Themis G2 300 equipped with an aberration correction and low-dose K2 camera. XPS was conducted with an ESCALAB250Xl spectrometer using Al Kα X-rays as the excitation source. AFM images were obtained using an OXFORD Cypher ES microscope in the tapping mode. FT-IR spectroscopy was carried out on RT-DLaTGS 27 spectrometer. GIXRD measurements were performed at the BL14B1 beamline of the Shanghai Synchrotron Radiation Facility (SSRF). The beam grazed the sample at an incidence angle of 0.14 degrees for 60 seconds with a beam energy of 10 keV. The distance between the sample and detector, as well as the scattering vector, was calibrated by lanthanum hexaboride, known as a polycrystalline material. The GIXRD patterns were processed by FIT-2D software. GIWAXS were performed on a Xeuss 2.0 SAXS/WAXS system (Xenocs SA, France). Cu Kα X-ray source (GeniX3D Cu ULD) generated at 50 kV and 0.6 mA was utilized to produce X-ray radiation with a wavelength of 1.5418 Å. A semiconductor detector (Pilatus 300 K, DECTRIS, Swiss) with a resolution of 487 × 619 pixels (pixel size = 172 × 172 μm^2) was used to collect the scattering signals.

DFT calculations

DFT calculations were performed by using the Vienna ab initio simulation Package[74,75]. We employed the Perdew-Burke-Ernzerhof generalized gradient approximation for the exchange-correlation functional[76], and the interaction between the ionic cores and valence electrons is treated by the projected augmented wave method[77]. To account for the weak vdW interaction between PyTTA (and TPA) and MoS_2, the DFT-D2 method has been adopted in our calculations[78]. The energy cutoff for the plane wave basis is set to be 400 eV. All the structures are relaxed until the force on each atom is less than 0.01 eV/Å with the energy converged to 10^{-6} eV. The distance between adjacent K-points in the Monkhorst-Pack scheme is set to be 0.03 Å^{-1}[79].

MD simulations

MD simulations were carried out by using the Large-scale Atomic/Molecular Massively Parallel Simulator (LAMMPS, https://www.lammps.org/). A ReaxFF-lg force field was modified to describe the interaction between atoms. This ReaxFF-lg force field was originally developed by Goddard et al. by adding a London dispersion term to the ReacFF force field, and it has been widely used in organic systems

containing C, H, O and N elements[80,81]. We have added the parameters for Cl in this ReaxFF-lg force field by referring to Strachan's study[82], which provided a ReaxFF force field for C-H-O-S-F-Cl systems.

Fabrication of COF/MoS2 heterojunction phototransistor

Bottom-gate bottom-contact phototransistors were fabricated on SiO_2/Si substrates with the doped Si substrate as the back gate and Au as the source-drain electrodes. SiO_2/Si chips with 30 nm Au source-drain electrodes on their surface were purchased from the Micro-Nano Fabrication Laboratory of Peking University. The thickness of the SiO_2 dielectric layer is 300 nm. MoS_2 film was transferred on the SiO_2/Si substrate. Then, the COF film was grown on it using the diffusion-limited synthesis strategy. The electrical properties were measured by a Keithley 4200SC semiconductor parameter analyzer. The measurements were carried out in a Glove box at room temperature.

Data availability

All data needed to evaluate the conclusions in the paper are present in the paper and/or the Supplementary Information. Source data are provided with this paper.

References

1. Guerette, P. et al. Accelerating the design of biomimetic materials by integrating RNA-seq with proteomics and materials science. *Nat. Biotechnol.* **31**, 908–915 (2013).
2. Ganewatta, M. S., Wang, Z. & Tang, C. Chemical syntheses of bioinspired and biomimetic polymers toward biobased materials. *Nat. Rev. Chem.* **5**, 753–772 (2021).
3. Gkoupidenis, P. et al. Organic mixed conductors for bioinspired electronics. *Nat. Rev. Mater.* **9**, 134–149 (2024).
4. Liu, Z. et al. Dual-bionic superwetting gears with liquid directional steering for oil-water separation. *Nat. Commun.* **14**, 4128 (2023).
5. He, Z. et al. An organic transistor with light intensity-dependent active photoadaptation. *Nat. Electron* **4**, 522–529 (2021).
6. Zhang, M. et al. An irradiance-adaptable near-infrared vertical heterojunction phototransistor. *Adv. Mater.* **34**, 2205679 (2022).
7. Xie, D. et al. Photoelectric visual adaptation based on 0D-$CsPbBr_3$-quantum-dots/2D-MoS_2 mixed-dimensional heterojunction transistor. *Adv. Funct. Mater.* **31**, 2010655 (2021).
8. Ding, S.-Y. & Wang, W. Covalent organic frameworks (COFs): from design to applications. *Chem. Soc. Rev.* **42**, 548–568 (2013).
9. Liang, R.-R., Jiang, S.-Y., A, R.-H. & Zhao, X. Two-dimensional covalent organic frameworks with hierarchical porosity. *Chem. Soc. Rev.* **49**, 3920–3951 (2020).
10. Lohse, M. S. & Bein, T. Covalent organic frameworks: structures, synthesis, and applications. *Adv. Funct. Mater.* **28**, 1705553 (2018).
11. Segura, J. L., Mancheño, M. J. & Zamora, F. Covalent organic frameworks based on Schiff-base chemistry: synthesis, properties and potential applications. *Chem. Soc. Rev.* **45**, 5635–5671 (2016).
12. Skorjanc, T., Shetty, D. & Valant, M. Covalent organic polymers and frameworks for fluorescence-based sensors. *ACS Sens.* **6**, 1461–1481 (2021).
13. Feng, L., Qian, C. & Zhao, Y. Recent advances in covalent organic framework-based nanosystems for bioimaging and therapeutic applications. *ACS Mater. Lett.* **2**, 1074–1092 (2020).
14. Scicluna, M. C. & Vella-Zarb, L. Evolution of nanocarrier drug-delivery systems and recent advancements in covalent organic framework–drug systems. *ACS Appl. Nano Mater.* **3**, 3097–3115 (2020).
15. Li, X. et al. Partitioning the interlayer space of covalent organic frameworks by embedding pseudorotaxanes in their backbones. *Nat. Chem.* **12**, 1115–1122 (2020).
16. Liu, K. et al. On-water surface synthesis of crystalline, few-layer two-dimensional polymers assisted by surfactant monolayers. *Nat. Chem.* **11**, 994–1000 (2019).
17. Samineni, L. & Kumar, M. Harnessing blue energy with COF membranes. *Nat. Nanotechnol.* **17**, 564–566 (2022).
18. Zhang, G. et al. Water-dispersible PEG-curcumin/amine-functionalized covalent organic framework nanocomposites as smart carriers for in vivo drug delivery. *Nat. Commun.* **9**, 2785 (2018).
19. Zhang, W. et al. Reconstructed covalent organic frameworks. *Nature* **604**, 72–79 (2022).
20. Ding, X. et al. Synthesis of metallophthalocyanine covalent organic frameworks that exhibit high carrier mobility and photoconductivity. *Angew. Chem. Int. Ed.* **50**, 1289–1293 (2011).
21. Wan, S. et al. Covalent organic frameworks with high charge carrier mobility. *Chem. Mater.* **23**, 4094–4097 (2011).
22. Ding, X. et al. An n-channel two-dimensional covalent organic framework. *J. Am. Chem. Soc.* **133**, 14510–14513 (2011).
23. Feldblyum, J. I. et al. Few-layer, large-area, 2D covalent organic framework semiconductor thin films. *Chem. Commun.* **51**, 13894–13897 (2015).
24. Yue, Y., Li, H., Chen, H. & Huang, N. Piperazine-linked covalent organic frameworks with high electrical conductivity. *J. Am. Chem. Soc.* **144**, 2873–2878 (2022).
25. Colson, J. W. & Dichtel, W. R. Rationally synthesized two-dimensional polymers. *Nat. Chem.* **5**, 453–465 (2013).
26. Cui, B. et al. Realization of lieb lattice in covalent-organic frameworks with tunable topology and magnetism. *Nat. Commun.* **11**, 66 (2020).
27. Evans, A. M. et al. Thermally conductive ultra-low-k dielectric layers based on two-dimensional covalent organic frameworks. *Nat. Mater.* **20**, 1142–1148 (2021).
28. Colson, J. W. et al. Oriented 2D covalent organic framework thin films on single-layer graphene. *Science* **332**, 228–231 (2011).
29. Sun, J. et al. A molecular pillar approach to grow vertical covalent organic framework nanosheets on graphene: hybrid materials for energy storage. *Angew. Chem. Int. Ed.* **57**, 1034–1038 (2018).
30. Sun, B. et al. Oriented covalent organic framework film on graphene for robust ambipolar vertical organic field-effect transistor. *Chem. Mater.* **29**, 4367–4374 (2017).
31. Xu, L. et al. Surface-confined single-layer covalent organic framework on single-layer graphene grown on copper foil. *Angew. Chem. Int. Ed.* **53**, 9564–9568 (2014).
32. Li, H. et al. Nucleation and growth of covalent organic frameworks from solution: the example of COF-5. *J. Am. Chem. Soc.* **139**, 16310–16318 (2017).
33. Yao, L. et al. Covalent organic framework nanoplates enable solution-processed crystalline nanofilms for photoelectrochemical hydrogen evolution. *J. Am. Chem. Soc.* **144**, 10291–10300 (2022).
34. Kim, S. & Choi, H. C. Recent advances in covalent organic frameworks for molecule-based two-dimensional materials. *ACS Omega* **5**, 948–958 (2020).
35. Côté, A. P. et al. Porous, crystalline, covalent organic frameworks. *Science* **310**, 1166–1170 (2005).
36. Jin, E. et al. Designed synthesis of stable light-emitting two-dimensional sp^2 carbon-conjugated covalent organic frameworks. *Nat. Commun.* **9**, 4143 (2018).
37. Evans, A. M. et al. Seeded growth of single-crystal two-dimensional covalent organic frameworks. *Science* **361**, 52–57 (2018).
38. Ma, T. et al. Single-crystal x-ray diffraction structures of covalent organic frameworks. *Science* **361**, 48–52 (2018).
39. Fan, C. et al. Scalable fabrication of crystalline COF membranes from amorphous polymeric membranes. *Angew. Chem. Int. Ed.* **60**, 18051–18058 (2021).
40. Gutzler, R. et al. Surface mediated synthesis of 2D covalent organic frameworks: 1,3,5-tris(4-bromophenyl)benzene on graphite (001), Cu (111), and Ag (110). *Chem. Commun.* 4456–4458 (2009).
41. Lafferentz, L. et al. Controlling on-surface polymerization by hierarchical and substrate-directed growth. *Nat. Chem.* **4**, 215–220 (2012).

42. Bieri, M. et al. Porous graphenes: two-dimensional polymer synthesis with atomic precision. *Chem. Commun.* **45**, 6919–6921 (2009).
43. Sahabudeen, H. et al. Wafer-sized multifunctional polyimine-based two-dimensional conjugated polymers with high mechanical stiffness. *Nat. Commun.* **7**, 13461 (2016).
44. Yang, Y. et al. A self-standing three-dimensional covalent organic framework film. *Nat. Commun.* **14**, 220 (2023).
45. Zhong, Y. et al. Wafer-scale synthesis of monolayer two-dimensional porphyrin polymers for hybrid superlattices. *Science* **366**, 1379–1384 (2019).
46. Yang, J. et al. Advancing osmotic power generation by covalent organic framework monolayer. *Nat. Nanotechnol.* **17**, 622–628 (2022).
47. Ciesielski, A. et al. Dynamic covalent chemistry of bisimines at the solid/liquid interface monitored by scanning tunnelling microscopy. *Nat. Chem.* **6**, 1017–1023 (2014).
48. DeBlase, C. R. et al. Rapid and efficient redox processes within 2D covalent organic framework thin films. *ACS Nano* **9**, 3178–3183 (2015).
49. Zhang, P. et al. Covalent organic framework nanofluidic membrane as a platform for highly sensitive bionic thermosensation. *Nat. Commun.* **12**, 1844 (2021).
50. Khan, N. A. et al. Solid–vapor interface engineered covalent organic framework membranes for molecular separation. *J. Am. Chem. Soc.* **142**, 13450 (2020).
51. Liu, M. et al. Two-dimensional covalent organic framework films prepared on various substrates through vapor induced conversion. *Nat. Commun.* **13**, 1411 (2022).
52. Khan, N. A. et al. Assembling covalent organic framework membranes via phase switching for ultrafast molecular transport. *Nat. Commun.* **13**, 3169 (2022).
53. Medina, D. D. et al. Room temperature synthesis of covalent-organic framework films through vapor-assisted conversion. *J. Am. Chem. Soc.* **137**, 1016 (2015).
54. Lv, Y. et al. An In situ film-to-film transformation approach toward highly crystalline covalent organic framework films. *CCS Chem.* **4**, 1519 (2022).
55. Zhou, Z. et al. Growth of single-crystal imine-linked covalent organic frameworks using amphiphilic amino-acid derivatives in water. *Nat. Chem.* **15**, 841–847 (2023).
56. Wang, M. Y. et al. Electrochemical interfacial polymerization toward ultrathin COF membranes for brine desalination. *Angew. Chem. Int. Ed.* **62**, e202219084 (2023).
57. Hong, J. et al. Solid-liquid interfacial engineered large-area two-dimensional covalent organic framework films. *Angew. Chem. Int. Ed.* **63**, e202317876 (2023).
58. Yuan, J. et al. Photo-tailored heterocrystalline covalent organic framework membranes for organics separation. *Nat. Commun.* **13**, 3826 (2022).
59. Das, G. et al. A polyrotaxanated covalent organic network based on viologen and cucurbit [7]uril. *Commun. Chem.* **2**, 106 (2019).
60. Liu, J. et al. Self-standing and flexible covalent organic framework (COF) membranes for molecular separation. *Sci. Adv.* **6**, 1110 (2020).
61. He, X. et al. De novo design of covalent organic framework membranes toward ultrafast anion transport. *Adv. Mater.* **32**, 2001284 (2020).
62. Du, W. et al. Ultrathin free-standing porous aromatic framework membranes for efficient anion transport. *Angew. Chem. Int. Ed.* **63**, e202402943 (2024).
63. Lei, Z. et al. Boosting lithium storage in covalent organic framework via activation of 14-electron redox chemistry. *Nat. Commun.* **9**, 576 (2018).
64. Dong, J., Zhang, L., Dai, X. & Ding, F. The epitaxy of 2D materials growth. *Nat. Commun.* **11**, 5862 (2020).
65. Liu, J. et al. On-liquid-gallium surface synthesis of ultrasmooth thin films of conductive metal–organic frameworks. *Nat. Synth.* **3**, 715–726 (2024).
66. Malhotra, R., Price, W. E., Woolf, L. A. & Easteal, A. J. Thermodynamic and transport properties of 1, 2-dichloroethane. *Int. J. Thermophys.* **11**, 835–861 (1990).
67. Brownell, W. E., Qian, F. & Anvari, B. Cell membrane tethers generate mechanical force in response to electrical stimulation. *Biophys. J.* **99**, 845–852 (2010).
68. Liao, F. et al. Bioinspired in-sensor visual adaptation for accurate perception. *Nat. Electron.* **5**, 84–91 (2022).
69. Monjezi, B. H. et al. Current trends in metal–organic and covalent organic framework membrane materials. *Angew. Chem. Int. Ed.* **60**, 15153 (2021).
70. Martínez-Periñán, E., Martínez-Fernández, M., Segura, J. L. & Lorenzo, E. Electrochemical (bio) sensors based on covalent organic frameworks (COFs). *Sensors* **22**, 4758 (2022).
71. Lee, J. et al. Monolayer optical memory cells based on artificial trap-mediated charge storage and release. *Nat. Commun.* **8**, 14734 (2017).
72. Nur, R. et al. High responsivity in MoS_2 phototransistors based on charge trapping HfO_2 dielectrics. *Chem. Mater.* **1**, 103 (2020).
73. Hu, J. et al. Sulfur vacancy-rich MoS_2 as a catalyst for the hydrogenation of CO_2 to methanol. *Nat. Catal.* **4**, 242–250 (2021).
74. Kresse, G. & Hafner, J. Ab initio molecular dynamics for open-shell transition metals. *Phys. Rev. B.* **48**, 13115 (1993).
75. Kresse, G. & Furthmüller, J. Efficiency of ab-initio total energy calculations for metals and semiconductors using a plane-wave basis set. *Comput. Mater. Sci.* **6**, 15 (1996).
76. Perdew, J. P., Burke, K. & Ernzerhof, M. Generalized gradient approximationmade simple. *Phys. Rev. Lett.* **77**, 3865 (1996).
77. Kresse, G. & Joubert, D. From ultrasoft pseudopotentials to the projector augmented-wave method. *Phys. Rev. B.* **59**, 1758 (1999).
78. Grimme, S. Semiempirical GGA-type density functional constructed with a long-range dispersion correction. *J. Comput. Chem.* **27**, 1787 (2006).
79. Monkhorst, H. J. & Pack, J. D. Special points for Brillouin-zone integrations. *Phys. Rev. B.* **13**, 5188 (1976).
80. Liu, L., Liu, Y., Zybin, S. V., Sun, H. & Goddard, W. A. ReaxFF-/g: correction of the reaxFF reactive force field for london dispersion, with applications to the equations of state for energetic materials. *J. Phys. Chem. A.* **115**, 11016 (2011).
81. Aktulga, H. M., Fogarty, J. C., Pandit, S. A. & Grama, A. Y. Parallel reactive molecular dynamics: numerical methods and algorithmic techniques. *Parallel Comput.* **38**, 245 (2012).
82. Wood, M. A., Van Duin, A. C. & Strachan, A. Coupled thermal and electromagnetic induced decomposition in the molecular explosive αHMX; a reactive molecular dynamics study. *J. Phys. Chem. A.* **118**, 885 (2014).

Acknowledgements

The authors acknowledge the financial support from the CAS Project for Young Scientists in Basic Research (No. YSBR-053), National Natural Science Foundation of China (52173211, 22173109), Beijing National Laboratory for Molecular Sciences (BNLMS) and the National Key R&D Program of China (2024YFE0109200). The authors acknowledge the SSRF for providing precious time and the synchrotron XRD facility at beamline NO. 14B/15U. X.X.Z. thanks to the Peking University startup funding and the National Natural Science Foundation of China (Grant No.52273279). The theoretical calculations were carried out on TianHe-1(A) at the National Supercomputer Center in Tianjin.

Author contributions

M.H. Liu and J.H. Kuang contributed equally. J.Y. Chen and Y.Q. Liu proposed and supervised the project. M.H. Liu designed and carried out the experiments. J.Y. Chen conceptualized the work and analyzed the data. M.H. Liu, J.H. Kuang, X.C. Han, Y.X. Liu, W.Q. Gao, S.C. Shang, X.Y. Wang, J.X. Hong, B. Guan, X.X. Zhao, Y.L. Guo, Z.Y. Zhao, Y. Zhao, and C. Liu performed characterization experiments. J.C. Dong carried out the theoretical calculations. J.Y. Chen, M.H. Liu, J.H. Kuang, and J.C. Dong wrote the manuscript. All the authors participated in discussions of the research.

Competing interests

The authors declare no conflicting interest.

Additional information

Supplementary information The online version contains supplementary material available at https://doi.org/10.1038/s41467-024-54844-4.

Correspondence and requests for materials should be addressed to Xiaoxu Zhao, Yunlong Guo, Jichen Dong or Jianyi Chen.

Peer review information *Nature Communications* thanks the anonymous, reviewer(s) for their contribution to the peer review of this work. A peer review file is available.